Unmanned Systems, Vol. 12, No. 2 (2024) 409–428

DOI: 10.1142/S230138502441019X

UNMANNED SYSTEMS
https://www.worldscientific.com/worldscinet/us

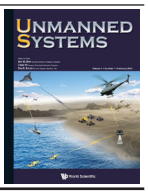

TJ-FlyingFish: An Unmanned Morphable Aerial–Aquatic Vehicle System

Xuchen Liu [*,†,††], Minghao Dou [*,†], Ruixin Yan [†], Dongyue Huang [*,†], Songqun Gao [†], Biao Wang [‡,‡‡], Jinqiang Cui [§], Qinyuan Ren [¶], Lihua Dou [‖], Zhi Gao [**], Jie Chen [*], Ben M. Chen [†,§§]

[*]*Shanghai Research Institute for Intelligent Autonomous Systems, Tongji University, Shanghai, P. R. China*

[†]*Department of Mechanical and Automation Engineering, The Chinese University of Hong Kong, Hong Kong, P. R. China*

[‡]*College of Automation Engineering, Nanjing University of Aeronautics and Astronautics, Nanjing, Jiangsu, P. R. China*

[§]*Peng Cheng Laboratory, Shenzhen, Guangdong, P. R. China*

[¶]*College of Control Science and Engineering, Zhejiang University, Hangzhou, Zhejiang, P. R. China*

[‖]*School of Automation, Beijing Institute of Technology, Beijing, P. R. China*

[**]*School of Remote Sensing and Information Engineering, Wuhan University, Wuhan, Hubei, P. R. China*

In this paper, we present in this work a fairly complete process for developing an unmanned aerial–aquatic vehicle system, TJ-FlyingFish, which includes an innovative design methodology of the aerial–aquatic platform and the cross-medium localization, dynamics modeling, and flight control systems. The development faces the challenge how to manipulate locomotion effectively in both water and air which presents substantial differences in fluid properties. Additionally, there are difficulties in perception and navigation because of the discontinuity of mediums. To cope with these challenges, we designed an innovative unmanned aerial–aquatic vehicle with an optimized dual-speed and tilting propulsion configuration. The rotors/propellers operate in different ranges of rotating speed in the two different mediums, providing sufficient thrust and ensuring output efficiency. Besides, thrust vectoring is achieved by rotating each propulsion unit around its mounted arm, facilitating agile underwater cruising. Another key component of our approach is a sophisticated multi-sensor-based cross-medium localization system that combines SLAM, sensor synchronization, and data capture mechanisms, enabling seamless transitions between aerial and aquatic environments, and supporting autonomous operations. The results are fully validated through actual flight experiments.

Keywords: Unmanned aerial– vehicles; cross-medium locomotion; cross-medium localization.

US

1. Introduction

Autonomous systems, including unmanned ground vehicles (UGVs), unmanned aerial vehicles (UAVs), unmanned surface vehicles (USVs), and unmanned underwater vehicles (UUVs), are poised to play pivotal roles in various industrial applications. These applications span from reconnaissance

Received 19 Ocotber 2023; Revised 22 December 2023; Accepted 22 December 2023; Published 9 February 2024. This paper was recommended for publication in its revised form by Special Issue Editors: Jie Chen, Ben M. Chen and Jie Huang.
Email Addresses: [††]*xcliu@mae.cuhk.edu.hk*, [‡‡]*billwang110@gmail.com; wangbiao@nuaa.edu.cn*, [§§]*bmchen@cuhk.edu.hk*
[‡‡]Corresponding author.

for search and rescue, security surveillance, environmental and traffic monitoring, powerline and pipeline inspections, building inspections, geographic mapping, tunnel inspections, film production, to logistic delivery and warehouse management, to name a few. The rapid development of autonomous unmanned vehicles has made them a key economic focus [1]. In this work, we concentrate on the development of an unmanned aerial–aquatic vehicle (UAAV) named TJ-FlyingFish.

Aerial–aquatic vehicles possess unique advantages due to their versatility in both aerial and underwater environments. In water, these vehicles can utilize buoyancy for efficient vertical movement, requiring less energy compared to aerial flight where lift must be generated to counteract gravity. Additionally, underwater operations offer natural cover and stealth due to decreased visibility caused by light refraction and dispersion. In contrast, the low air density results in reduced drag, making high-speed travel more effective than in water. Aerial–aquatic vehicles can leverage these characteristics to exploit the strengths of both mediums while mitigating each other's limitations. These distinctive capabilities make aerial–aquatic vehicles well-suited for various applications, including surveillance, inspection, search and rescue, and environmental monitoring.

Designing a multimodal vehicle, especially regarding locomotion and propulsion, poses challenges due to the distinct properties of different mediums. Moving in fluid mediums such as air and water needs three-dimensional (3D) navigation, as opposed to terrestrial motion that occurs primarily on a two-dimensional plane defined by the land's topography. Various vehicle designs, such as fixed-wing aircraft and multirotor craft for aerial operations, and boats and submersibles for aquatic environments, have individually addressed these requirements. However, seamlessly integrating these features into a single vehicle is not always straightforward or intuitive.

Recently, a variety of functionalized prototypes [2, 3] have been demonstrated, including fixed-wing [4], multirotor [5–7], fixed-wing-multirotor hybrid [8–10], morphable [11, 12], and biologically inspired [13] designs. While there are platforms designed for different fluid environments [6] for multirotor-based prototypes, the majority of them are simply standard aerial hardware constructions with water resistance, which don't have the same level of mobility in water as they do in the air. Another choice is to connect submerged and airborne platforms [14, 15], which affects aerial capacity by increasing the airborne load.

A morphable quadrotor was proposed in [16] that enables coupled symmetric thrust vectoring accomplished through straightforward mechanical connections, increasing the vehicle's mobility on the surface and under water to some extent. However, designing the attitude controller remains challenging due to strong hydrodynamic coupling and prototype under-actuation. Motors and propellers for aerial applications are used in the propulsion system to operate in both air and water while sacrificing air performance for underwater functionality [17].

The primary objectives of this study are to simplify controller design and enhance propulsion system performance through structural modifications. As depicted in Fig. 1, TJ-FlyingFish incorporates an independent tilting mechanism for thrust vectoring instead of a coupled symmetric one. This design choice offers increased flexibility in thruster configurations, eliminates the constraints imposed by the original coupling mechanism on controller design, and potentially makes the prototype an over-actuated vehicle. Additionally, for propulsion, the dual-speed gearbox driven by the motor forward and reverse is equipped with two working intervals for different fluid environments, enhancing underwater propulsion even further.

Operating these vehicles across different mediums autonomously poses a unique challenge for localization and navigation. Transitioning between air and water introduces perceptual discontinuities, compounded by specialized sensors optimized for one medium or the other. Accurate and reliable localization is crucial, especially for autonomous operations. Traditional localization methods, designed primarily for single-medium operations, struggle in cross-medium scenarios. To fill this gap, this paper presents a multi-sensor-based cross-medium localization

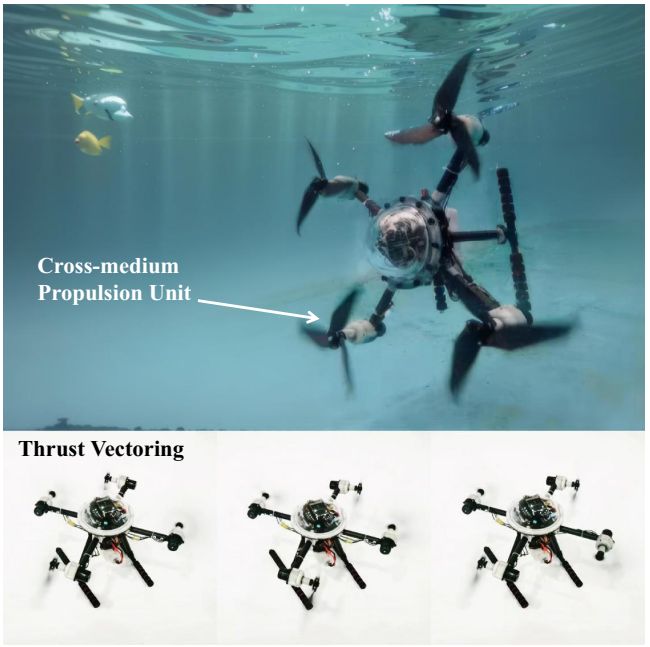

Fig. 1. TJ-FlyingFish: An unmanned aerial-aquatic vehicle.

approach, utilizing cutting-edge SLAM techniques, precise sensor synchronization, and efficient data acquisition methods to ensure consistent localization across mediums.

We claim that a preliminary version of this paper was previously presented in [18]. Compared to the initial conference paper, this paper includes an analytical model of the prototype and discusses the extended development for automatic cross-medium operation. The principal contributions of this work can be summarized as follows:

(1) A prototype equipped with tiltable propulsion units is proposed. Agile locomotion across various mediums is facilitated by these dual-mode propulsion units and an independent thrust vectoring mechanism.
(2) A cross-medium localization system is developed, utilizing a multi-sensor fusion strategy.
(3) A comprehensive analytical model, applicable in both aerial and underwater conditions, is derived.
(4) Finally, the attitude and position control scheme is designed based on thrust vectoring. Furthermore, automatic switching operation is realized for the cross-medium system.

The remaining sections of this paper are outlined as follows. Section 2 presents the concept of TJ-FlyingFish, highlighting the challenges involved in designing the aerial-aquatic system and the corresponding methodology to address them. In Sec. 3, we provide an overview of the prototype, covering the mechanical design and the avionic system. The cross-medium localization system is described in Sec. 4. The dynamic model of the UAAV and automatic control strategies are then presented in Sec. 5, whereas the performance of both manual and automatic operation, along with the results of cross-medium localization, are illustrated in Sec. 6. Finally, we draw some concluding remarks in Sec. 7.

2. UAAV Design Concept

2.1. *Design methodology*

In comparison to vehicles that can only operate in one medium, aerial–aquatic hybrid vehicles must consider the following concerns in order to improve their ability to operate in multiple mediums.

(1) **Cross-medium propulsion:** Need to generate enough airlift against gravity and produce enough underwater propulsion, and reduce overall weight to improve propulsion efficiency across both mediums.
(2) **Thruster configurations:** Need to configure the rational arrangement of thrusters to overcome gravity and hydrodynamic resistance in the air and water, respectively.
(3) **Cross-medium localization:** Need to combine sensors with aerial and aquatic capabilities with data fusion for seamless localization.
(4) **Lightweight waterproofing:** Need to reduce the weight of the waterproof construction to ease the workload on the aerial operation while maintaining tightness and stability in water.

To address the first issue, the disparate demands placed on the operating point of the propulsion system by the vast difference in density and viscosity of the two mediums must be addressed. The mass flow created by the propulsion unit determines the magnitude of the propulsion force. Fast sparse air flow should be provided by high-speed propellers for aerial conditions, while slow dense water flow should be generated by high-torque propellers. To improve the performance of a cross-medium propulsion system, the motor and propeller must be torque-matched in two different working ranges in order to achieve the aforementioned output characteristics.

Hydrodynamics includes additional components such as buoyancy, added mass, and hydrodynamic drag, which necessitates design consideration of the second issue. Thrusters are oriented vertically upwards in standard multirotors to resist gravity, and yaw motion is driven by anti-torque from propeller rotating, which can be coupled with vertical motion in the body frame and sluggish underwater. Surge or sway motion is created by tilting the fuselage and directing small thrust portions into the horizon. Because of buoyancy and hydrodynamic drag, the fuselage must be tilted at a large angle to direct the majority of thrust to the horizontal direction and achieve the desired horizontal motion, as demonstrated in [6]. Large-angle tilting has three disadvantages: first, its dynamic response underwater is obtuse due to added mass and hydrodynamic drag; second, the linear model based on the assumption of a small attitude angle fails; and third, it obstructs sensors, necessitating multiple sensor mounts. Thrusters for underwater vehicles are typically laid out in the direction of motion to translate with direct output and yaw with differential output, making vehicle mobility difficult to achieve. To achieve efficient motion in both mediums, the aerial–aquatic vehicle must have the aforementioned features.

There are very few sensors capable of cross-medium localization from both the air and the sea. The GPS technology commonly used in the air cannot penetrate the water due to signal constraints. Furthermore, optical positioning methods used in the air are influenced by underwater visibility and illumination conditions, resulting in poor performance. Underwater sound sensors, which are widely used underwater, are completely useless in the air and add unnecessary aerial weight due to their size. These sensors should be activated selectively based on the

medium environment, and a data fusion system to calculate real-time position should be developed.

In terms of waterproofing design, the joint surface smoothness and stiffness determine the platform's sealability, and the underwater stability can be achieved through neutral buoyancy design and inherent restoring torque provided by the center of gravity and buoyancy margin. To meet the lightweight requirements, solutions based on materials and structures, such as rapid prototyping [19], have been investigated. The prototype in this study is lightweight at the expense of some sealability, with a maximum dive depth of 3 m guaranteed.

2.2. *Aerial–aquatic propulsion unit*

There are three ways to deal with the torque matching issue for propulsion systems used in two different mediums. The first involves setting up separate propulsion systems for aerial and underwater environments, which can offer excellent performance in both mediums but add an enormous workload [15]. The solution is to use a single set of aerial motors and propellers to accommodate both mediums [7]. The problem, though, is that increasing the ability for propulsion in one medium inevitably means sacrificing that ability in the other. The final method uses one motor to drive two transmission chains for different medium environments and switches between them in time, including driving two propellers directly [4] and driving one propeller through a gearbox at variable speed range [20]. This method is acceptable in weight and offers better propulsion in both water and air but has the disadvantage of a complex structure that could result in high operating losses and unreliability.

The developed prototype adopts the third option mentioned above, which uses a dual-speed gearbox to drive one propeller. The gearbox uses a differential planetary gear transmission with fewer teeth to increase reliability while reducing complexity and weight (the entire propulsion unit weighs 122 g including the motor and propeller). Figures 2(a) and 2(b) show the schematic diagram of the working principle. When the motor is rotating forward, the blue chain transmits torque, which is output directly for aerial mode. When the motor is rotating backward, the red chain transmits torque, which is output with more torque for underwater mode. Figures 2(c) and 2(d) show the structure inside and its appearance, respectively. This design has been tested in a prototype. Section 6.1 will discuss how it performs.

2.3. *Independent thrust vectoring*

Similar to the propulsion scheme, there are three possible solutions for the thruster configuration: (i) to use two propulsion systems for different mediums operating simultaneously [15]; (ii) to use the aerial propulsion system directly underwater; and lastly (iii) to use a group of propulsion systems with variable structures and change the thruster configuration as needed.

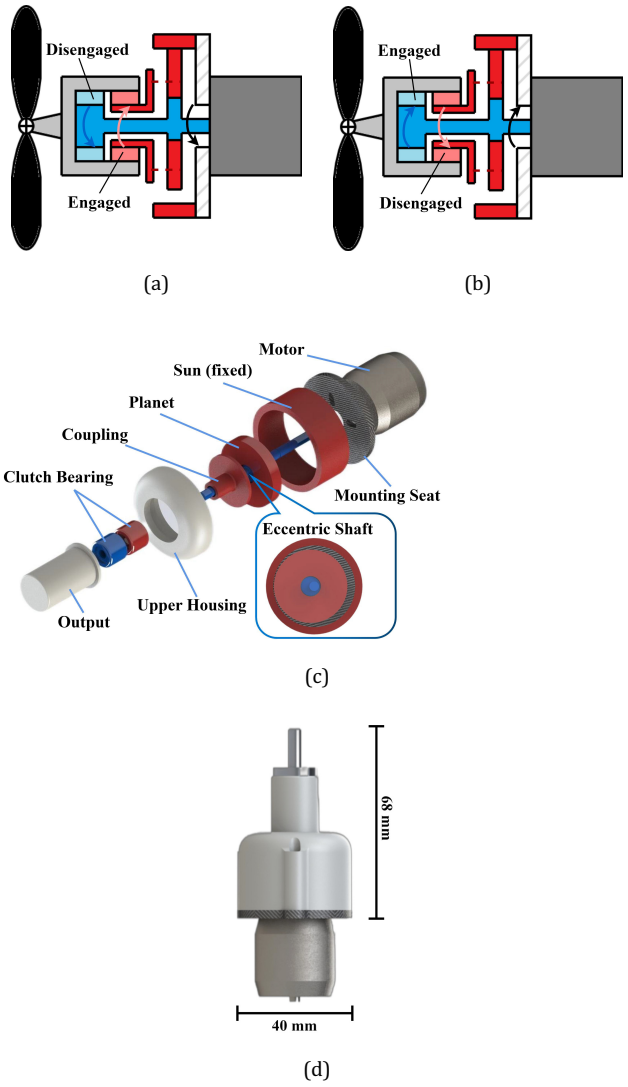

Fig. 2. Propulsion unit.

The thrust vectoring on a single propulsion system is how we propose to change the configuration, which has the advantages of greater system integration and lighter weight. In earlier research, the vehicle's coupled symmetric thrust vectoring mechanism offers a dive mode and an angled mode that makes underwater movement easier. Due to the margin between the center of gravity and the action point of the total thrust [21], it might be challenging to decouple the thrusts produced by each propulsion unit and assign them to a single degree of freedom when using the coupled symmetric method. Each propulsion unit has been altered

to spin independently around its mounting arm to vectorize thrusts in order to address this. This design enables both modes based on the original symmetric method and more complex modes to investigate underwater mobility strategies.

A tilt angle mixing approach is designed to generate surge, sway, and yaw motions to demonstrate the ability of four vectorized thrusters driven separately and working cooperatively. Figure 3 illustrates such mixing which can be expressed in the following formula:

$$\begin{bmatrix}\beta_1\\ \beta_2\\ \beta_3\\ \beta_4\end{bmatrix} = \frac{a\pi}{2}\left\{S\left(\begin{bmatrix}-1 & 1 & -1\\ 1 & -1 & -1\\ 1 & 1 & -1\\ -1 & -1 & -1\end{bmatrix}\begin{bmatrix}J_{\text{surge}}\\ J_{\text{sway}}\\ J_{\text{yaw}}\end{bmatrix}\right) - \begin{bmatrix}1\\ 1\\ 1\\ 1\end{bmatrix}\right\}, \tag{1}$$

where $S(x)$ is the sigmoid function that, combined with $a = 1$ or $a = -1$, limits the angle to the range $(0, \pi)$ and $(-\pi, 0)$, partitioning the operational range of the vectorized thrust into two working zones, lower and upper, and J_* indicates the joystick volume for the surge, sway, and yaw channels.

The vehicle's maneuverability in cross-medium environments has been significantly improved by the new design in the two aforementioned aspects. The analytical model will be used in Sec. 5 to analyze the particular effects and functionalities, and Sec. 6 will cover the actual implementation and results.

2.4. *Multi-sensor fusion localization*

The multi-sensor-based localization strategy is manifested in Fig. 5. We introduce two concurrent algorithms, each tailored to distinct tasks, to ensure robust cross-medium localization. The primary algorithm focuses on pose estimation pertinent to control tasks. Accurate, high-frequency, and low-latency pose estimations are of paramount importance for such tasks. We employ the well-established Extended Kalman Filter algorithm to amalgamate data from various sensors. This approach facilitates a high-frequency, low-latency pose estimation, thus bolstering the robustness of the control tasks. Within this context, the emphasis isn't predominantly on high-frequency or low-latency but rather on mitigating sensor-induced errors and the prolonged accumulation and drift of these errors. Such concerns directly influence the efficacy of the navigation algorithm. To address sensor malfunction, we implement bespoke algorithms to either pre-process or discard faulty measurements contingent on the sensor type.

It should be noted that vision sensors and early intervention are imperative to augment measurement accuracy. Upon obtaining raw data from the vision sensor, it undergoes a preprocessing and enhancement phase. Subsequently, all sensor data is appraised by a status manager to assess the reliability of its measurements. For instance, with vision sensors, the quantity of matched feature points and their consistency across successive frames serve as primary indicators in assessing potential data degradation. In the case of DVL, the congruence of measurements from its four transducers becomes the principal criterion to ascertain potential sensor degradation. Upon this evaluation, any aberrant sensor measurements are discarded or compensated. The consolidated data is then sent to the tightly coupled sensor fusion algorithm, which employs factor graph optimization techniques to achieve precise system pose estimation. This resultant pose estimation is subsequently employed in executing tasks, notably navigation. To guarantee the robustness of the system, it's imperative to highlight that two distinct algorithms are executed on separate computing platforms. This design ensures their independence, preventing any potential interference between the two.

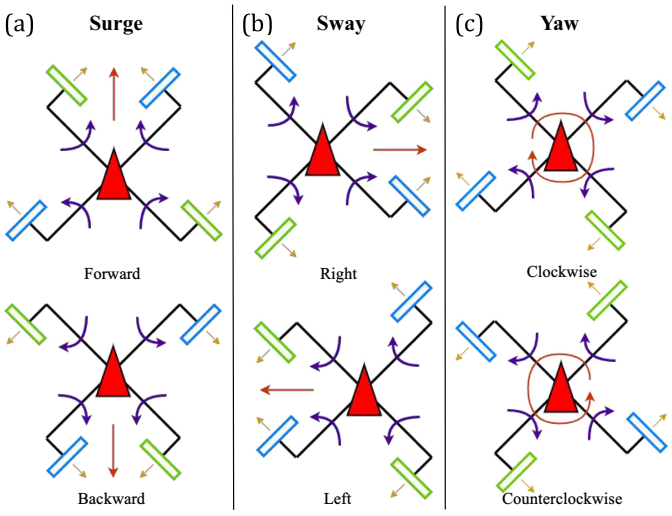

Fig. 3. The schematic diagram of the tilt angle allocation.

3. Design of Unmanned Aerial–Aquatic Vehicle Platform

To test the feasibility of the proposed concept in Sec. 2, a quadrotor prototype with independently tiltable propulsion units was built. Table 1 presents the design parameters. It has a 380 mm wheelbase and a weight of 1.63 kg (aerial thrust to weight ratio: 3.75), and it can hover in the air for 6 min or cruise underwater for 40 min. It is made up of four major parts: four independently-operating arm-tilting mechanisms located in the center of the fuselage; four propulsion units installed at the ends of the arms; two waterproof cabins located at the top and bottom of the

Table 1. Design parameters.

Description	Value
Mass	1.63 kg
Wheelbase	380 mm
Propeller Size	9.4 inch
Aerial endurance	5 min 50 s
Aquatic endurance (Hovering)	around 40 min
Maximum diving depth	3 m

tilting mechanisms to house the avionics system; and a waterproof battery cabin located at the bottom of the fuselage. Figure 4(a) shows each component in exploded view. Furthermore, the control algorithm based on PX4 is designed to be under-buoyant in order to be suspended in water. A cornerstone of the vehicle's design is the ability to accurately and reliably localize itself in both aerial and underwater environments. Ensuring seamless transitions between these mediums necessitates innovative design considerations.

3.1. *Mechanical design*

A similar mechanism can be found in the aerial fully actuated multi-rotor [22], which is typically mounted at the end of the fixed arm and drives the rotor directly for tilting. Because the propulsion unit is located at the end of the arm, such a design cannot be implemented in the prototype because it would concentrate more mass at the end of the arm, increasing rotational inertia and impairing the flight effect. As a result, the tilting mechanism is optimally mounted inside the body, as shown in Fig. 4(a).

However, the tilting torque is delivered to the propulsion unit via the arm rather than directly, resulting in a somewhat long drive chain. This could introduce vibration to the entire system during operation if the structural clearance exists, resulting in energy loss and a possible controller collapse. To address this, three bearings are used to support the tilt structure, as shown in Fig. 4(a), in order to ensure rigidity and eliminate the clearance with redundant support. The tilting arm is made of a carbon fiber tube with an internal coupling to the servo and bushings that attach to ceramic bearings. Finally, the above-mentioned components are secured into shells before being forced together by the upper and lower carbon fiber covers, which also help to attach the waterproof cabins and other components.

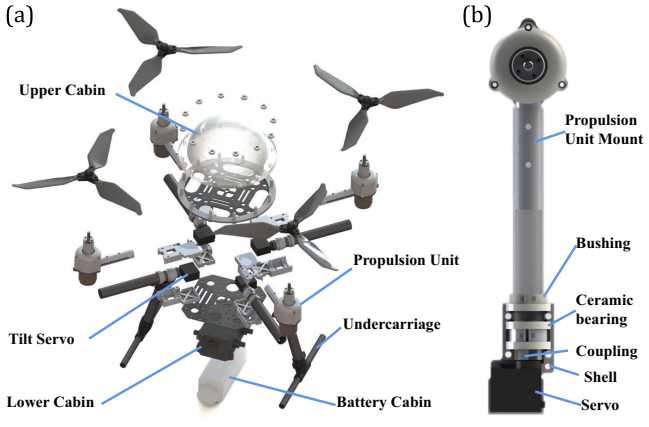

Fig. 4. The structure of TJ-FlyingFish.

3.2. *Avionic system*

Table 2 lists the prototype's components, and Fig. 5 depicts their wiring. The prototype is outfitted with a 433 MHz telemetry radio that can be used to monitor the prototype's status and change parameters in real-time up to a depth of 2 m underwater. To ensure the stability and penetration of the remote control signal underwater, a 900 MHz radio system is used, which typically operates up to 1.5 m deep. A 4-in-1 BLHeli32 ESC controls the four motors forward and backward using a Dshot 1200 signal and sends the propulsion unit's real-time status to the Pixhawk 4 mini.

An external integrated depth gauge records the current depth status. A 9V BEC is used to power four high-voltage servos which can produce 0.6Nm torque. A switching circuit powered by a MOSFET and a 5V BEC prevents the waterproof structure from being repeatedly disassembled and reassembled while the vehicle is powered on or off.

This prototype requires three additional channels (SURGE, SWAY, and YAW2) in addition to the standard

Table 2. Selected components.

Components	Parameters
Motor	T-MOTOR AT2312-KV1150
Propeller	DJI 9455 × 3
Electrical Speed Controller (ESC)	FOXEER 45A
Battery	TATTU LiPo 4S 2200 mAh
Flight Controller	Pixhawk4 mini
Telemetry Radio	433MHz Holybro SiK V3
Transmitter	Taranis X-Lite Pro
Receiver	900MHz Frsky R9 Mini-OTA
Power Module	Holybro PM02
Battery Elimination Circuit (BEC)	MAMBA 5V/9V 2A
Servo	KINGMAX KM0950MDHV
MOS Field-Effect Transistor (MOSFET)	LR7843
Depth gauge	MS5837 pressure sensor

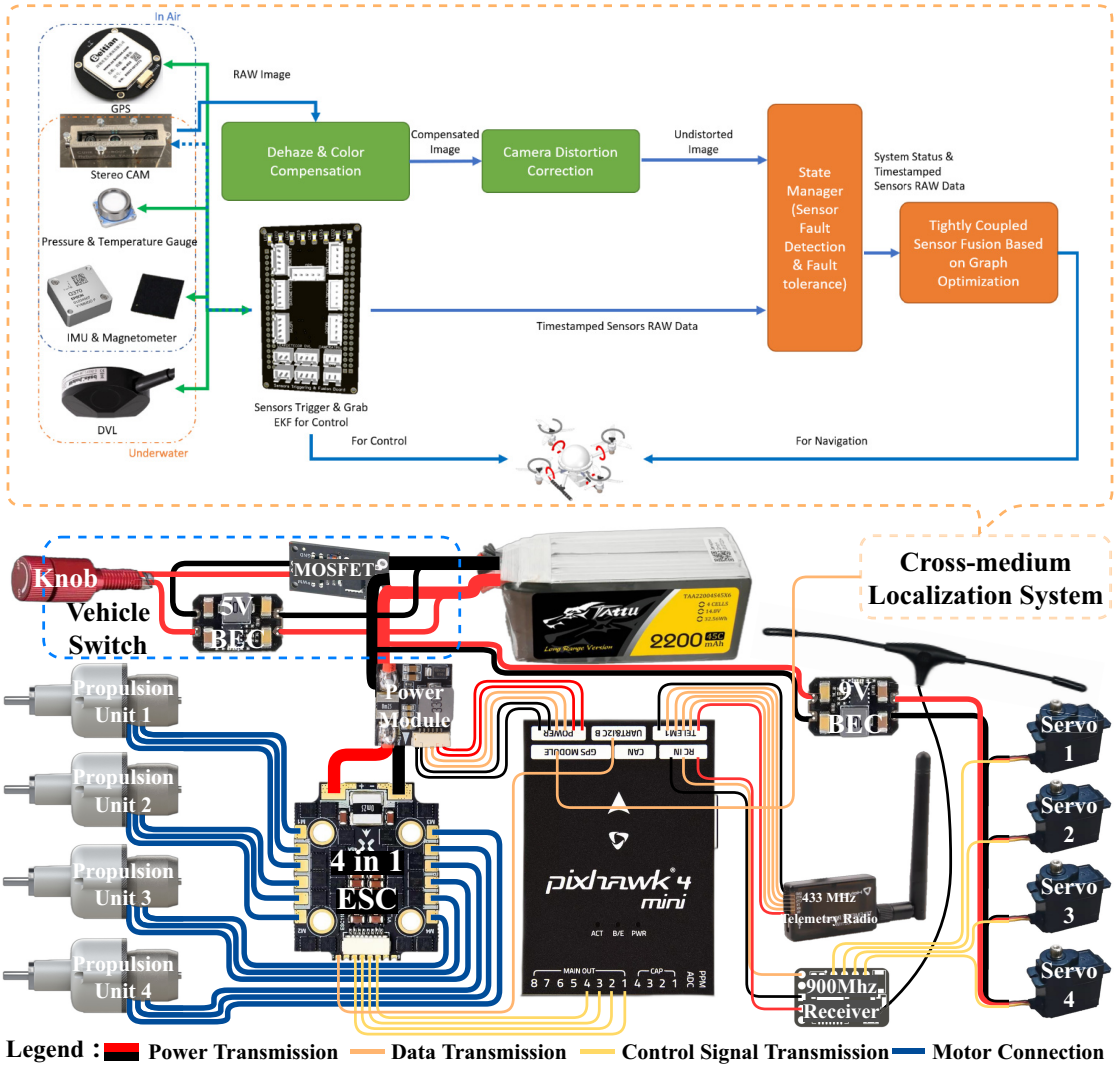

Fig. 5. The schematic diagram of the proposed prototype and localization system, and the data flow diagram of the cross-medium localization system.

quadrotor's attitude control channels (ROLL, PITCH, and YAW1). This is due to the addition of independent thrust vectoring. In contrast to YAW2, which creates the yaw motion through thrust vectoring, YAW1 completes the yaw motion through torque. We chose the Frsky X-Lite Pro with an integrated gyroscope because a typical transmitter would have trouble managing so many channels at once. GyroX and GyroY are given the ROLL and PITCH channels, respectively, and the top buttons are given the YAW1 channel, enabling the inactive use of three joysticks to control the SURGE, SWAY, and YAW2 channels. The precise remote control channel mappings are shown in Fig. 6.

The propeller and motor matching issue in the underwater condition has changed due to the development of the gearbox into the transmission ratio design issue, which is related to the performance requirement of the aerial condition in the selection of motor and propeller. The DJI 9455×3 three-bladed carbon fiber propeller and the T-MOTOR AT2312-KV1150 motor, powered by a 4S LiPo battery, were both carefully selected for the flight. The ideal gear ratio for the above motor and propeller underwater is

CH	Mapping
1	THROTTLE
2	YAW2 (by thrust vectoring)
3	SURGE
4	SWAY
5	ROLL
6	PITCH
7	ARM
8	PROPULSION MODE SWITCH
9 & 10	YAW1 (by torque)

Fig. 6. The channel mapping on Frsky Taranis X-Lite Pro transmitter.

established as 12.33 through QPROP simulation analysis in accordance with the procedure described in [20].

4. Cross-medium Localization

Effective localization for aerial–aquatic vehicles presents unique challenges, especially during transition across mediums. The discontinuity across mediums coupled with the specificity of sensors necessitates a robust and adaptable localization system. Our design addresses these challenges head-on, leveraging a combination of sensors and methodologies. In this study, the task of environmental sensing was accomplished through the use of six different sensors: a manometer, a digital compass, a camera, a DVL, an IMU, and a GPS.

4.1. *Sensor selection*

When entering water, environmental conditions change immediately and significantly, resulting in degraded image quality. This is mainly due to the decrease of landmarks, which increases the complexity of acquisition and height-related data. In addition, these challenges are further amplified facing wave interference and low-frequency vibration. In particular, relying solely on measurement from the IMU and the pressure gauge would increase the margin of error and make the collected data unreliable.

To solve the above problem, a DVL can be applied. It is able to determine the relative speed and height with respect to the seabed based on Doppler effect. The data are then used to bound the calculations based on IMUs and manometers, thereby improving the reliability and accuracy of underwater data. In order to successfully perform cross-medium robot state estimation, sensor selection based on current environmental conditions becomes important. Since the special refraction properties of water may impede the camera's field of view, it is necessary to reduce the computational burden associated with pose estimation. Therefore, we chose the Intel RealSense D435i stereo camera as the main vision sensor. The camera is characterized by two sets of intrinsic parameters for the compensation of image distortion, one for underwater environment and another for aerial environment. They are obtained by separate calibration procedures offline and switched in real-time during the transition.

In the event of significant environmental degradation, maintaining uninterrupted state estimation requires the deployment of a highly accurate IMU. Because IMU sensors exhibit unique environmental independence, they exhibit consistent behavior under degraded conditions. In addition, the electronic compass provides reliable and accurate heading information whether the robot is in the air or underwater. In order to estimate altitude over different mediums, traditional barometers cannot work properly underwater. Therefore, we chose a gel-type manometer, which can effectively estimate external pressure, whether atmospheric or hydrostatic. The integration of redundant pressure gauges with appropriate compensation algorithms can successfully solve the problem of dynamic pressure changes. To determine the absolute position of the robot in water and in the air, we used a multi-mode satellite navigation module. It is capable of simultaneously receiving signals from GPS, GALILEO, BDS, and GLONASS.

4.2. *Data acquisition and synchronization*

Due to the inherent way these sensors operate, the frequency of data acquisition will vary. In addition, the inherent electrical properties of these sensors may inadvertently introduce delays in the data retrieval process. Such differences can lead to inaccuracies in the robot's state estimation, and in certain cases can lead to the failure of SLAM systems. Therefore, in this project, the acquisition of stable, frequency-synchronized, and latency-free sensor data is a key cornerstone for the stable operation of the SLAM system. Accurate sensor synchronization and data acquisition are not just pivotal for consistent localization; they play a foundational role in the successful implementation of SLAM. Any discrepancies or delays in sensor data can compromise the SLAM system's accuracy, underscoring the importance of our synchronization methodologies.

In general, there are two ways to solve the problems of multi-sensor data delay and synchronization. The first method involves both offline and online sensor calibration by calculating the time delay. Depending on the nature of the delay and the sensor data, interpolation or integration techniques are used to obtain the observation data of the robot within a specific time. However, this approach has a significant disadvantage as it requires a significant investment of time and resources in both offline and online calibration during system operation. In addition, the accuracy of the robot's state estimation depends on the algorithm's ability to handle sensor data delays.

Another approach involves generating a hardware trigger signal that uses this external trigger to precisely synchronize different sensors. This method only requires an MCU to generate trigger signals in different intervals, thus starting different sensors. It effectively eases the computational effort to adapt algorithms with different sensor data characteristics (thus facilitating sensor replacement) and simultaneously reduces the number of offline and online calibration tasks. The generation of the trigger signal of the

sensor requires the generation of continuous, synchronous square-wave signals with different frequencies. It can be realized by using an MCU timer. The data of the sensor is resolved in real-time through the relevant interface given a time stamp. This provides a solid foundation for the stable work of the following localization algorithm. The data from our localization system seamlessly integrates with the avionic system. This synchronized data flow is crucial for real-time flight control, navigation, and other autonomous operations, ensuring the vehicle's stable and effective operation in both mediums.

In addressing the present challenge, our project harnesses the Timer functionality inherent in the STM32 Microcontroller Unit (MCU) to generate precise sensor trigger signals, thereby enhancing the quality of the resultant electrical signal performance. Concurrently, the MCU receives a substantial volume of sensor data. By sequencing this data in conjunction with the trigger frequency, we can ensure that the sensor alignment remains unaffected by the temporal aspects of the data reception by the MCU. Moreover, we employ an Extended Kalman Filter to integrate the sensor data gathered within the MCU, guaranteeing real-time estimation of the system's state. All these functionalities have been amalgamated into a Sensor Triggering and Fusion Board, are shown in Fig. 7.

4.3. *Robust localization using EKF*

The Extended Kalman Filter (EKF) is at the heart of our localization system, offering a probabilistic framework that integrates real-time sensor measurements to estimate the robot's state. EKF is computationally efficient and can provide immediate state estimations, crucial for real-time operations. Additionally, the EKFs robustness to initialization conditions ensures that it remains reliable even in challenging environments.

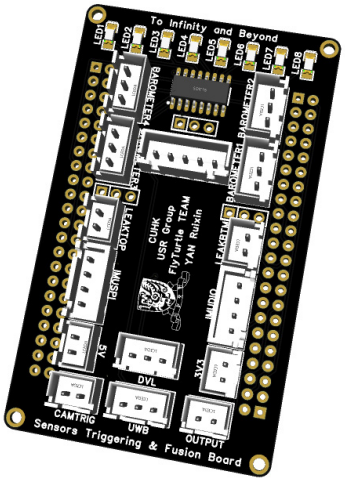

Fig. 7. The sensor trigger and fusion board.

One of the key challenges addressed by our EKF-based approach is ensuring synchronicity of sensor data. Given the tight integration of sensor measurements in the EKF, any asynchronicity can corrupt the estimations. Fortunately, we have solved the problem in the last subsection.

Furthermore, our system leverages both the EKF and Factor Graph Optimization (FGO). While the EKF provides swift and efficient state estimations, the FGO complements it by offering global optimality and precision, ensuring that our robot is localized with the highest accuracy possible. In what follows, is the objective function of the FGO:

$$\min_{\boldsymbol{X}} \left\{ \begin{array}{l} \left\| \mathbf{r}_p - \mathbf{H}_p \boldsymbol{X} \right\|^2 + \sum\limits_{k \in [1,n]} \left\| \mathbf{r}_{\text{Pre}} \left(\tilde{\boldsymbol{z}}_{k-1,k}^{\text{Pre}}, \boldsymbol{X} \right) \right\|_{k-1,k}^{2} \\ \quad + \sum\limits_{h \in [0,m]} \left\| \mathbf{r}_{\text{Press}} \left(\tilde{\boldsymbol{z}}_{h}^{\text{Press}}, \boldsymbol{X} \right) \right\|_{h}^{2} \\ \quad + \sum\limits_{h \in [0,m]} \left\| \mathbf{r}_{\text{DVL}} \left(\tilde{\boldsymbol{z}}_{h}^{\text{DVL}}, \boldsymbol{X} \right) \right\|_{h}^{2} \end{array} \right\}. \quad (2)$$

where the pairing $\{\boldsymbol{r}_p, \boldsymbol{H}_p\}$ indicates the prior information obtained through marginalization, $\boldsymbol{r}_{\text{Pre}}$ denotes the residuals derived from the IMU pre-integration measurements, $\boldsymbol{r}_{\text{Press}}$ signifies the residuals from the pressure gauge measurements, $\boldsymbol{r}_{\text{DVL}}$ pertains to the residuals of the DVL measurements. In addition, the symbol m stands for the total number of DVL measurements observed in the sliding window, and n stands for IMU.

4.4. *Tightly coupled high-precision localization*

Building upon the robust foundation provided by the EKF, our system further refines localization by tightly coupling the data from all sensors. This tight integration allows for real-time cross-validation of data, ensuring any discrepancies are immediately addressed. The result is not just high-precision localization but also the ability to construct detailed and accurate maps of the environment. This is crucial for tasks that require the robot to be aware of its surroundings, such as obstacle avoidance or path planning.

This integration emphasizes the dual approach: first, ensuring robustness through EKF, and then refining accuracy through tight coupling. This progression from robustness to precision paints a clear picture of the system's capabilities and the layered strategy employed to achieve its goals.

5. Dynamics Modeling and Control Design

It should be noted that preliminary results of dynamics modeling of TJ-FlyingFish have been reported in [23, 24].

To describe vehicle motion, a local North-East-Down (NED) coordinate system $\mathcal{F}_{\mathrm{n}}$ is used for navigation reference. The body-axis coordinate system $\mathcal{F}_{\mathrm{b}}$ is used to represent the orientation of the vehicle with respect to the NED coordinate system. Its origin O_{b} is located at its Center of Gravity (CoG). Then, the following notations are introduced to express the translational and rotational motions:

$$\begin{aligned} &\boldsymbol{p}_{\mathrm{n}} = [x, y, z]^{\mathrm{T}}, \quad \boldsymbol{\varphi} = [\phi, \theta, \psi]^{\mathrm{T}}, \quad \boldsymbol{\eta} = \begin{bmatrix} \boldsymbol{p}_{\mathrm{n}} \\ \boldsymbol{\varphi} \end{bmatrix}, \\ &\boldsymbol{v}_{\mathrm{b}} = [u, v, w]^{\mathrm{T}}, \quad \omega_{\mathrm{b}} = [p, q, r]^{\mathrm{T}}, \quad \boldsymbol{\nu} = \begin{bmatrix} \boldsymbol{v}_{\mathrm{b}} \\ \omega_{\mathrm{b}} \end{bmatrix}, \end{aligned} \tag{3}$$

where $\boldsymbol{p}_{\mathrm{n}}$ and $\boldsymbol{\varphi}$ are the position and orientation of the vehicle in $\mathcal{F}_{\mathrm{n}}$, $\boldsymbol{v}_{\mathrm{b}}$ and ω_{b} are the linear and angular velocity described in $\mathcal{F}_{\mathrm{b}}$, respectively.

The kinematics equation of the vehicle in both air and water mediums can be expressed uniformly in the vector-matrix form as

$$\dot{\boldsymbol{\eta}} = \begin{bmatrix} \boldsymbol{R}_{\mathrm{n/b}} & 0_{3\times 3} \\ \boldsymbol{0_{3\times 3}} & \boldsymbol{S^{-1}} \end{bmatrix} \boldsymbol{\nu}, \tag{4}$$

where $\boldsymbol{R}_{\mathrm{n/b}}$ is the rotational matrix from the body frame to the NED frame, and $\boldsymbol{S}^{-1}$ is a lumped transformation matrix, which are given as follows:

$$\boldsymbol{R}_{\mathrm{n/b}} = \begin{bmatrix} \mathrm{c}_\theta \mathrm{c}_\psi & \mathrm{s}_\phi \mathrm{s}_\theta \mathrm{c}_\psi - \mathrm{c}_\phi \mathrm{s}_\psi & \mathrm{c}_\phi \mathrm{s}_\theta \mathrm{c}_\psi + \mathrm{s}_\phi \mathrm{s}_\psi \\ \mathrm{c}_\theta \mathrm{s}_\psi & \mathrm{s}_\phi \mathrm{s}_\theta \mathrm{c}_\psi + \mathrm{c}_\phi \mathrm{c}_\psi & \mathrm{c}_\phi \mathrm{s}_\theta \mathrm{s}_\psi - \mathrm{s}_\phi \mathrm{c}_\psi \\ -\mathrm{s}_\theta & \mathrm{s}_\phi \mathrm{c}_\theta & \mathrm{c}_\phi \mathrm{c}_\theta \end{bmatrix}, \tag{5}$$

$$\boldsymbol{S}^{-1} = \begin{bmatrix} 1 & \mathrm{s}_\phi \mathrm{t}_\theta & \mathrm{c}_\phi \mathrm{t}_\theta \\ 0 & \mathrm{c}_\phi & -\mathrm{s}_\phi \\ 0 & \mathrm{s}_\phi / \mathrm{c}_\theta & \mathrm{c}_\phi / \mathrm{c}_\theta \end{bmatrix}, \tag{6}$$

where $\mathrm{s}_* = \sin(*)$, $\mathrm{c}_* = \cos(*)$ and $\mathrm{t}_* = \tan(*)$.

The kinetics equation of the vehicle in both air and water mediums can be then generally expressed as

$$\boldsymbol{M}_* \dot{\boldsymbol{\nu}} + \boldsymbol{C}_*(\boldsymbol{\nu})\boldsymbol{\nu} + \boldsymbol{D}_*(\boldsymbol{\nu})\boldsymbol{\nu} + \boldsymbol{G}_*(\boldsymbol{\eta}) = \boldsymbol{f}, \tag{7}$$

where the subscript $*$ selected as 'ae' is for the aerial mode, 'aq' is for the aquatic mode, $\boldsymbol{M}_*$ is the inertia matrix, $\boldsymbol{C}_*(\boldsymbol{\nu})$ is the Coriolis-centripetal matrix, $\boldsymbol{D}_*(\boldsymbol{\nu})$ is the damping matrix, $\boldsymbol{G}_*(\boldsymbol{\eta})$ is the general restoring force produced by gravity and buoyancy, and $\boldsymbol{f}$ represents the vectored propulsive force.

5.1. *Aerial mode*

In aerial domain, the terms of (7) are as for usual quadrotor UAVs. The matrix $\boldsymbol{M}_*$ for the inertia term is

$$\boldsymbol{M}_{\mathrm{ae}} = \mathrm{diag}(m, m, m, I_{xx}, I_{yy}, I_{zz}), \tag{8}$$

where m is the mass of the vehicle, I_{xx}, I_{yy}, I_{zz} are the moments of inertia of the vehicle around the body axes. The matrix $\boldsymbol{C}_*(\boldsymbol{\nu})$ for the Coriolis-centripetal term is

$$\boldsymbol{C}_{\mathrm{ae}}(\boldsymbol{\nu}) = \begin{bmatrix} 0 & 0 & 0 & 0 & -mw & mv \\ 0 & 0 & 0 & mw & 0 & -mu \\ 0 & 0 & 0 & -mv & mu & 0 \\ 0 & -mw & mv & 0 & -I_{zz}r & I_{yy}q \\ mw & 0 & -mu & I_{zz}r & 0 & -I_{xx}p \\ -mv & mu & 0 & -I_{yy}q & I_{xx}p & 0 \end{bmatrix}. \tag{9}$$

For the matrix $\boldsymbol{D}_*(\boldsymbol{\nu})$ of the damping term, the linear damping has little influence on the overall dynamics, and the quadratic damping is dominant in aerodynamics. Hence, it can be formulated as

$$\begin{aligned} \boldsymbol{D}_{\mathrm{ae}}(\boldsymbol{\nu}) = -\frac{1}{2}\rho\ \mathrm{diag}(&D_{x2}|u|, D_{y2}|v|, D_{z2}|w|, \\ &D_{l2}|p|, D_{m2}|q|, D_{n2}|r|), \end{aligned} \tag{10}$$

where ρ is the air density, D_{x2}, D_{y2}, D_{z2}, D_{l2}, D_{m2}, D_{n2} are the drag constants.

The general restoring force produced by the airsteam is weak and eliminated in the aerial mode. Hence, it can be simplified into

$$\boldsymbol{G}_{\mathrm{ae}}(\boldsymbol{\eta}) = \begin{bmatrix} W\mathrm{s}_\theta \\ -W\mathrm{c}_\theta \mathrm{s}_\phi \\ -W\mathrm{c}_\theta \mathrm{c}_\phi \\ 0 \\ 0 \\ 0 \end{bmatrix}, \tag{11}$$

where $W = mg$ is the weight of the vehicle with g the gravitational acceleration.

5.2. *Aquatic mode*

For the underwater environment, hydrodynamics is in effect. Apart from the body motion parameters as in the air, the effects of added mass and damping need be considered carefully [25]. For simplicity, the coupling of the added mass and damping cross operating channels, as well as the influence of the tilting propulsion units on the overall vehicle dynamics, is ignored temporarily. The relevant aquatic components are defined according to the standard quadrotor layout ($\beta_i = -\frac{\pi}{2}$), and a similar result using the Center of Buoyancy (CoB) as the origin can be seen in [26].

In this case, the matrix $\boldsymbol{M}_{\mathrm{aq}}$ includes the part $\boldsymbol{M}_{\mathrm{ae}}$ and the added mass part $\boldsymbol{M}_{\mathrm{A}}$,

$$\begin{aligned} &\boldsymbol{M}_{\mathrm{aq}} = \boldsymbol{M}_{\mathrm{ae}} + \boldsymbol{M}_{\mathrm{A}}, \\ &\boldsymbol{M}_{\mathrm{A}} = \mathrm{diag}(X_{\dot{u}}, Y_{\dot{v}}, Z_{\dot{w}}, L_{\dot{p}}, M_{\dot{q}}, N_{\dot{r}}), \end{aligned} \tag{12}$$

where $X_{\dot{u}}$, $Y_{\dot{v}}$, $Z_{\dot{w}}$, $L_{\dot{p}}$, $M_{\dot{q}}$, $N_{\dot{r}}$ are added mass coefficients as shown in Table 3. Similarly, the Coriolis-centripetal matrix

$\boldsymbol{C}_{\mathrm{aq}}(\boldsymbol{\nu})$ includes the part $\boldsymbol{C}_{\mathrm{ae}}$ and the added mass part $\boldsymbol{C}_{\mathrm{A}}$,

$$\boldsymbol{C}_{\mathrm{aq}}(\boldsymbol{\nu}) = \boldsymbol{C}_{\mathrm{ae}}(\boldsymbol{\nu}) + \boldsymbol{C}_{\mathrm{A}}(\boldsymbol{\nu}),$$

$$\boldsymbol{C}_{\mathrm{A}}(\boldsymbol{\nu}) = \begin{bmatrix} 0 & 0 & 0 & 0 & Z_{\dot{w}}w & -Y_{\dot{v}}v \\ 0 & 0 & 0 & -Z_{\dot{w}}w & 0 & X_{\dot{u}}u \\ 0 & 0 & 0 & Y_{\dot{v}}v & -X_{\dot{u}}u & 0 \\ 0 & Z_{\dot{w}}w & -Y_{\dot{v}}v & 0 & N_{\dot{r}}r & -M_{\dot{q}}q \\ -Z_{\dot{w}}w & 0 & X_{\dot{u}}u & -N_{\dot{r}}r & 0 & L_{\dot{p}}p \\ Y_{\dot{v}}v & -X_{\dot{u}}u & 0 & M_{\dot{q}}q & -L_{\dot{p}}p & 0 \end{bmatrix}. \tag{13}$$

Noted that the damping term $\boldsymbol{D}_{\mathrm{aq}}(\boldsymbol{\nu})$ is composed of linear term $\boldsymbol{D}_{\mathrm{aqL}}$ and quadratic term $\boldsymbol{D}_{\mathrm{aqQ}}(\boldsymbol{\nu})$, which can be expressed as

$$\begin{aligned} \boldsymbol{D}_{\mathrm{aq}}(\boldsymbol{\nu}) &= \boldsymbol{D}_{\mathrm{aqL}} + \boldsymbol{D}_{\mathrm{aqQ}}(\boldsymbol{\nu}), \\ \boldsymbol{D}_{\mathrm{aqL}} &= -\mathrm{diag}(X_{u1}, Y_{v1}, Z_{w1}, L_{p1}, M_{q1}, N_{r1}), \\ \boldsymbol{D}_{\mathrm{aqQ}}(\boldsymbol{\nu}) &= -\mathrm{diag}(X_{u2}|u|, Y_{v2}|v|, Z_{w2}|w|, \\ &\quad L_{p2}|p|, M_{q2}|q|, N_{r2}|r|), \end{aligned} \tag{14}$$

where the coefficients are as shown in Table 3.

As the origin is pegged at the CoG, the general restoring force $\boldsymbol{G}_{\mathrm{aq}}(\boldsymbol{\eta})$ is expressed as

$$\boldsymbol{G}_{\mathrm{aq}}(\boldsymbol{\eta}) = \begin{bmatrix} (W-B)s_\theta \\ -(W-B)c_\theta s_\phi \\ -(W-B)c_\theta c_\phi \\ y_B B c_\theta c_\phi - z_B B c_\theta s_\phi \\ -z_B B s_\theta - x_B B c_\theta c_\phi \\ x_B B c_\theta s_\phi + y_B B s_\theta \end{bmatrix}, \tag{15}$$

Table 3. Notations of hydrodynamic coefficients.

	Surge	Sway	Heave	Roll	Pitch	Yaw
Added Mass	$X_{\dot{u}}$	$Y_{\dot{v}}$	$Z_{\dot{w}}$	$L_{\dot{p}}$	$M_{\dot{q}}$	$N_{\dot{r}}$
Linear Damping	X_{u1}	Y_{v1}	Z_{w1}	L_{p1}	M_{q1}	N_{r1}
Quadratic Damping	X_{u2}	Y_{v2}	Z_{w2}	L_{p2}	M_{q2}	N_{r2}

where $B = \rho g V$ is the buoyancy with ρ the water density and V is the displacement volume of the vehicle, $\boldsymbol{L}_B = [x_B, y_B, z_B]^{\mathrm{T}}$ represent the displacement of the CoB from the CoG.

5.3. *Vectorized propulsion*

To analyze the tilting effect of the propulsion unit, the coordinate system $\mathcal{F}_{\mathrm{p}_i}$ is defined attached to the ith ($i = 1, \ldots, 4$) propulsion unit, with the origin attached on the intersection of the tilting axis and the propeller shaft. As shown in Fig. 8, x_{p_i}-axis represents the tilting axis pointing outward along the arm, z_{p_i}-axis is aligned with the propeller shaft pointing opposite direction of the thrust T_i. By denoting the tilt angle of the propulsion unit with β_i and the mounting angle of the arm with δ_i, the axis vector $\boldsymbol{z}_{\mathrm{p}_i}$ and the position vector $\boldsymbol{o}_{\mathrm{p}_i}$ of the origin O_{p_i} can be expressed in the body frame $\mathcal{F}_{\mathrm{b}}$ as

$$\boldsymbol{z}_{\mathrm{p}_i} = [c_{\beta_i} c_{\delta_i}, c_{\beta_i} s_{\delta_i}, -s_{\beta_i}]^{\mathrm{T}}, \tag{16}$$

$$\boldsymbol{o}_{\mathrm{p}_i} = [-L_p s_{\delta_i}, L_p c_{\delta_i}, -H_p]^{\mathrm{T}}, \tag{17}$$

where L_p and H_p show the horizontal and vertical displacements between the origins of $\mathcal{F}_{\mathrm{b}}$ and $\mathcal{F}_{\mathrm{p}_i}$.

Subsequently, the vectorized propulsive force of (7) can be divided into the thrust part and the moment part as

$$\boldsymbol{T}_i = -T_i \boldsymbol{z}_{\mathrm{p}_i} = [-T_i c_{\beta_i} c_{\delta_i}, -T_i c_{\beta_i} s_{\delta_i}, T_i s_{\beta_i}]^{\mathrm{T}}, \tag{18}$$

$$\begin{aligned} \boldsymbol{M}_i &= b\tau_i \boldsymbol{z}_{\mathrm{p}_i} + \boldsymbol{o}_{\mathrm{p}_i} \times (-T_i \boldsymbol{z}_{\mathrm{p}_i}) \\ &= \begin{bmatrix} b\tau_i c_{\delta_i} c_{\beta_i} + T_i L_p c_{\delta_i} s_{\beta_i} - T_i H_p s_{\delta_i} c_{\beta_i} \\ b\tau_i s_{\delta_i} c_{\beta_i} + T_i L_p s_{\delta_i} s_{\beta_i} + T_i H_p c_{\delta_i} c_{\beta_i} \\ -b\tau_i s_{\beta_i} + T_i L_p c_{\beta_i} \end{bmatrix}, \end{aligned} \tag{19}$$

where T_i and τ_i are the thrust and anti-torque produced by the ith propulsion unit, respectively, b is a torque direction

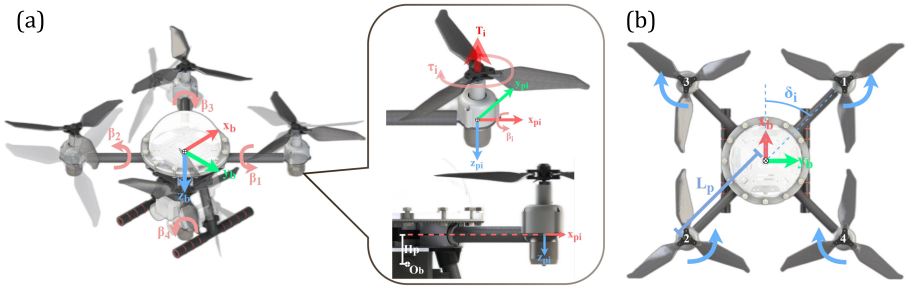

Fig. 8. Coordinate system definitions and layout of propulsion units.

scalar which yields

$$b = \begin{cases} 1, & \text{if } i = 1, 2, \\ -1, & \text{if } i = 3, 4. \end{cases} \tag{20}$$

Taking into account the introduction of the gearbox, the thrust T_i and torque τ_i generated by the ith propulsion unit is

$$T_i = \tilde{K}_T \omega_i^2 = \frac{K_T^* \omega_i^2}{(r^*)^2}, \tag{21}$$

$$\tau_i = \tilde{K}_\tau \omega_i^2 = \frac{K_\tau^* \omega_i^2}{(r^*)^2}, \tag{22}$$

where ω_i is the rotational speed of the ith motor, K_T^* and K_τ^* ($* = $ ae or aq) are the thrust and torque coefficients of the propeller in the air or water, r^* is the corresponding gear ratio, $\tilde{K}_T$ and $\tilde{K}_\tau$ are their calculated equivalent coefficients.

The vectorized propulsive force of (7), $\boldsymbol{f} = [T_x, T_y, T_z, M_{\text{roll}}, M_{\text{pitch}}, M_{\text{yaw}}]^{\text{T}}$, concerning every individual propulsion unit, can be calculated as

$$\boldsymbol{f} = \sum_{i=1}^{4} \begin{bmatrix} \boldsymbol{T}_i \\ \boldsymbol{M}_i \end{bmatrix} = \boldsymbol{K}\boldsymbol{\Omega}, \tag{23}$$

where $\boldsymbol{K} = [\boldsymbol{k}_x, \boldsymbol{k}_y, \boldsymbol{k}_z, \boldsymbol{k}_{\text{roll}}, \boldsymbol{k}_{\text{pitch}}, \boldsymbol{k}_{\text{yaw}}]^T$ is the geometrical coefficient matrix, and $\boldsymbol{\Omega} = [\omega_1^2, \omega_2^2, \omega_3^2, \omega_4^2]^{\text{T}}$ is composed of the squares of the rotational speed of motors. Additionally, the previously mentioned problem of the conventional multirotor's poor underwater yaw motion performance as well as the advantages of thrust vectoring can be examined as follows.

In water, the vehicle is intended to be roughly neutrally buoyant. It means that we usually balance the buoyancy and the weight of the vehicle by design so that it can float in water statically without disturbance. In the situation, all the motors are stopped, which is different from the hovering motion in the air. Suppose that we increase the speed of rotor 1 and rotor 2 (who rotate in the same direction) with the speed of rotor 3 and rotor 4 maintaining zeros to manipulate the yaw motion by anti-torque generated by rotor 1 and rotor 2. For usual quadrotor layout, $\boldsymbol{k}_{\text{yaw}} = [\tilde{K}_{\text{M}}, \tilde{K}_{\text{M}}, -\tilde{K}_{\text{M}}, -\tilde{K}_{\text{M}}]^{\text{T}}$. Yawing motion with level attitude is achieved by the speed output of motors: $\boldsymbol{\Omega} = [(\bar{\omega} + \Delta\omega)^2, (\bar{\omega} + \Delta\omega)^2, \bar{\omega}^2, \bar{\omega}^2]^{\text{T}}$. The total yawing moment in this situation is $M_{\text{yaw}} = 2\tilde{K}_{\text{M}} \Delta\omega^2$ with $\bar{\omega} = 0$. In the sametime, we have also the total thrust $T_z = 2\tilde{k}_{\text{T}} \Delta\omega^2$ since $\boldsymbol{k}_z = [\tilde{K}_{\text{T}}, \tilde{K}_{\text{T}}, \tilde{K}_{\text{T}}, \tilde{K}_{\text{T}}]^{\text{T}}$, which will unbalance the vertical motion. It means that the yaw motion may inadvertently cause z-direction motion underwater. Therefore, yaw motion and vertical motion cannot be decoupled in water as a conventional quadrotor does in the air where T_z is used to counteract gravity. One of the solutions to the coupling problem is to use vectorized propulsion.

For thrust vectoring, $\boldsymbol{k}_z = \tilde{K}_{\text{T}} \text{s}_{\beta_i} [1, 1, 1, 1]^{\text{T}}$ and $\boldsymbol{k}_{\text{yaw}} = (\tilde{K}_{\text{M}} \text{s}_{\beta_i} + \tilde{K}_{\text{T}} L_p \text{c}_{\beta_i})[1, 1, -1, -1]^{\text{T}}$. Yawing movement can be realized with $\beta_i = 0$ or π, which leads to $M_{\text{yaw}} = 4\tilde{K}_{\text{T}} L_p \bar{\omega}^2$ and $T_z = 0$ with $\boldsymbol{\Omega} = [\bar{\omega}^2, \bar{\omega}^2, \bar{\omega}^2, \bar{\omega}^2]^{\text{T}}$. Because $\tilde{K}_T$ is many orders of magnitude greater than $\tilde{K}_M$, the total yawing moment can be significantly increased. It means that the motion produced by T_z and M_{yaw} is decoupled. As shown experimentally in Sec. 6.3, thrust vectoring enables faster yaw motion during suspension in water.

5.4. *Attitude control*

The attitude control is built on the PX4 firmware's cascaded PID controller. For aerial operation, the original cascaded PID controller is deployed, and for aquatic, the developed control algorithm with thrust vectoring is implemented. To address the geometric changes caused by tilting the propulsion units, a dynamic mixer, as shown in Fig. 9, has been designed to replace the static one.

The duty cycle of motors can be obtained by mapping the desired speed of motors, and the desired speed is calculated by the moment and thrust input setpoints as

$$\vec{\boldsymbol{\Omega}} = \begin{bmatrix} \mathbf{k}_z^{\text{T}}(\beta_1, \beta_2, \beta_3, \beta_4) \\ \boldsymbol{k}_{\text{roll}}^{\text{T}}(\beta_1, \beta_2, \beta_3, \beta_4) \\ \boldsymbol{k}_{\text{pitch}}^{\text{T}}(\beta_1, \beta_2, \beta_3, \beta_4) \\ \boldsymbol{k}_{\text{yaw}}^{\text{T}}(\beta_1, \beta_2, \beta_3, \beta_4) \end{bmatrix}^{-1} \begin{bmatrix} T_z \\ 0 \\ 0 \\ 0 \end{bmatrix} = \boldsymbol{\xi} \begin{bmatrix} T_z \\ 0 \\ 0 \\ 0 \end{bmatrix}, \tag{24}$$

where the dynamic mixer $\boldsymbol{\xi}$ is derived by the inversion of the geometrical coefficient matrix in Eq. (23), and the desired attitude is set as zero input. Under such conditions, the lateral thrust is generated as

$$\begin{bmatrix} T_x \\ T_y \end{bmatrix} = \begin{bmatrix} \boldsymbol{k}_x^{\text{T}}(\beta_1, \beta_2, \beta_3, \beta_4) \\ \boldsymbol{k}_y^{\text{T}}(\beta_1, \beta_2, \beta_3, \beta_4) \end{bmatrix} \vec{\boldsymbol{\Omega}}, \tag{25}$$

which allows horizontal motion without rotating the fuselage.

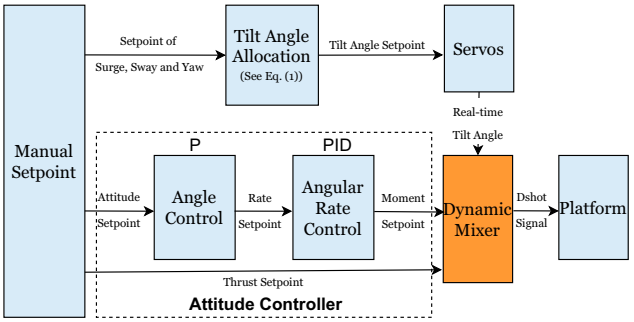

Fig. 9. Attitude control scheme by thrust vectoring.

The geometric coefficient matrix is calculated at a rate of 10 Hz in the PX4 firmware to implement the dynamic mixer $\boldsymbol{\xi}$. To avoid a singularity in the geometric coefficient matrix, the tilt angles of the propulsion units are limited to the range of $[\pi/6, 5\pi/6]$. Apart from that, the functionality shown on PX4 keeps without any additional development. The vehicle can stay in stable underwater in a small range of tilt angle of the propulsion units which thanks to the robustness of the controller although the perturbation of attitude is unavoidable with a static mixer. In fact, using the dynamic mixer to account for the effect of propulsion tilting, the tilt range can be significantly large because the perturbation is compensated. The final implementation result is shown in Sec. 6.3, along with a comparison of the maneuverability of the proposed dynamic mixer with that of a conventional quadrotor.

5.5. *Position control*

The position control does not use the aforementioned dynamic mixer since more work needs to be done on the position-attitude-decoupled controller before such a mixer can be adapted. As an alternative, the control algorithm for aquatic operation deploys a static mixer for the opposing quadrotor configuration ($\beta_i = -\frac{\pi}{2}$), while the original mixer ($\beta_i = \frac{\pi}{2}$) is employed for aerial operation, as shown in Fig. 10. Additionally, by forward feeding the real-time setpoints into the controller, an online trajectory generator — which is developed from the PX4 inherent motion planning function — is used to implement automatic underwater cruising. The trajectory generator calculates the intended position and velocity based on the vehicle's real-time states and connects subsequent pairs of waypoints using smoothed straight-line odometry [27]. The implementation results are given in Sec. 6.5.

6. Experimental Results

The independent thrust vectoring strategy and the cross-medium propulsion unit both contribute to this work. The propulsion capability is evaluated by the static output characteristics, and in order to gauge their improvement in aerial and aquatic locomotion, the aquatic maneuverability is by comparison with the conventional multirotor. Additionally, the water/air transition and underwater automated cruising are checked for operation together with the localization algorithm.

6.1. *Static output characteristics of the propulsion unit*

The propulsion test stand, as depicted in Fig. 11, is designed to evaluate the propulsion unit's actual performance. The 6-axis force balance (Maxwell F6D3934) used in the test is not waterproof, so in order to connect the propulsion unit to the balance and measure force and moment output above the water's surface, a cantilever beam structure made of three carbon fiber tubes is used. Additionally, the TT100 thruster made by TT robotics, which has an operating power almost identical to that of the propulsion unit, is employed to compare the performance of the propulsion unit to that of a traditional underwater thruster.

Figures 12(a)–12(c) illustrate their static output characteristics. The efficiency of the motor together with the gearbox is defined by the ratio of shaft power (shaft torque, Q multiplied by angular speed, ω) to electrical power (input voltage, V multiplied by input current, I):

$$\eta_{\mathrm{M}} = Q\omega/VI, \tag{26}$$

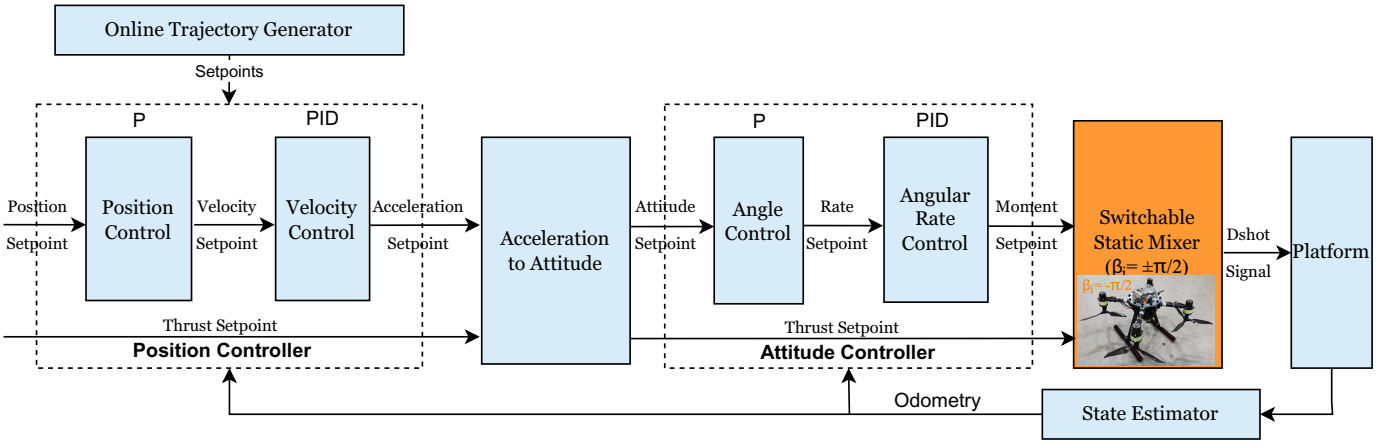

Fig. 10. Position control scheme.

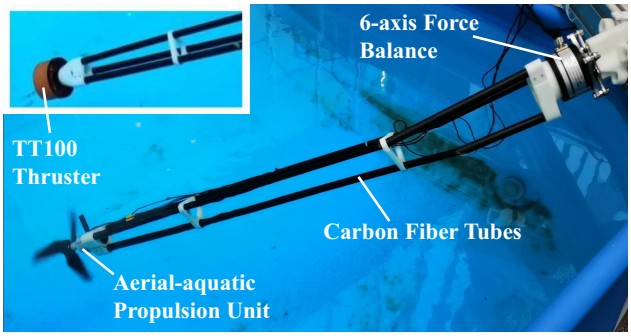

Fig. 11. The structure of the propulsion test stand, and tested propulsion system.

and specific thrust is defined by the ratio of output thrust, T to electrical power:

$$\bar{T} = T/VI. \tag{27}$$

While the specific thrust of these two is comparable, the aquatic efficiency η_M of the TT100 is greater than that of the propulsion unit (AT2312 with gearbox). The above result indirectly suggests that the aerial propeller can also achieve high efficiency when used underwater, which has been confirmed by simulation in [20] and by experiment in [6]. Specific thrust measures the combined efficiency of the motor and propeller. Due to the open structure of the gearbox and the lengthy transmission chain used in aquatic mode, which increases internal friction and hydrodynamic resistance, testing data shows an unavoidable loss of internal efficiency of 5.1% in aerial operation and 21.3% in aquatic conditions. Although this is the case, the gearbox structure still increases the motor's operational efficiency, total and specific thrust, and expands the operating range from 30% to 100% duty circle. Additionally, its 45g lightweight prevents the air from being overly burdened, ensuring aerial performance.

A comparison of the propulsion systems found in other aerial-aquatic vehicles is shown in Table 4. The AquaMAV [20], which has a better thrust-to-weight ratio but subpar static output characteristics, employs a similar concept. The MAAQuad [16] and the Loon-copter [6] operate on the same principle they are propelled underwater by aerial propulsion and only perform better than the proposal in the air. The thrust-to-weight ratio of the Nezha-mini is reduced thanks to two separate systems that provide excellent performance in both mediums. The proposed scheme performs better when efficiency, weight, and output thrust are taken into account all at once.

6.2. *Aquatic–aerial transition performance*

Propeller-induced air entrainment creates substantial variability in the phase fraction of the operating medium during the aquatic–aerial transition [28], resulting in a very unstable flow field that renders it difficult for the vehicle to transition from water to air. To understand the influence of this mechanism on the propulsion unit and the vehicle, a high-speed camera is employed to capture the entire transition process, and average motor rotational speed, ESC output power, and vehicle depth are recorded simultaneously.

The mechanism of the whole transition process can be summarized in Fig. 13 and the process is captured by a high-speed camera (Fig. 14(a)), where each condition can be reflected in Figs. 14(b)–14(d). In Fig. 14(b), when the vehicle is manually manipulated to rise to the water surface at a certain speed, the propeller will be lifted out of the water to the air due to inertia, which allows a certain acceleration time for rotation. Following that, if the throttle is large enough, the propeller will be accelerated to provide enough thrust to completely extricate itself from water and

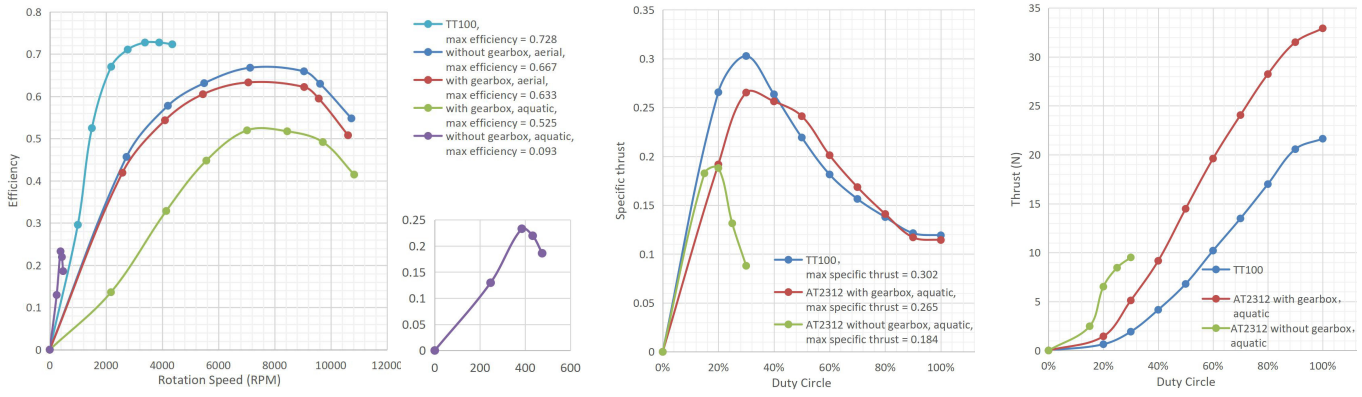

(a) (b) (c)

Fig. 12. Comparison of the static performance: (a) The efficiency of the motor. (b) and (c): The specific thrust and thrust of the whole propulsion system.

Table 4. Comparison of aerial–aquatic propulsion systems.

	Aerial Efficiency	Aquatic Efficiency	Max Aquatic Specific Thrust	Max Aquatic Thrust-to-Weight Ratio
Proposed	63.3%	52.5%	0.265	$32N/122g = 0.262$
AquaMAV [20]	50.0%	46.0%	0.172	$9.5N/28g = 0.339$
MAAQuad [16]	12.3% (simulated)	unknown	0.4 (simulated)	$4.8N/19.3g = 0.249$ (simulated)
Loon-copter [6]	unknown	unknown	0.18	$12N/130.4g = 0.092$
Nezha-mini [15]	unknown	unknown	≈ 0.27	$15N/83.4g = 0.180$
TT100	—	72.8%	0.302	$21.6N/290g = 0.075$

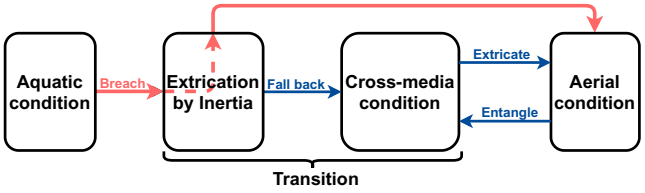

Fig. 13. Aquatic–Aerial transition mechanism.

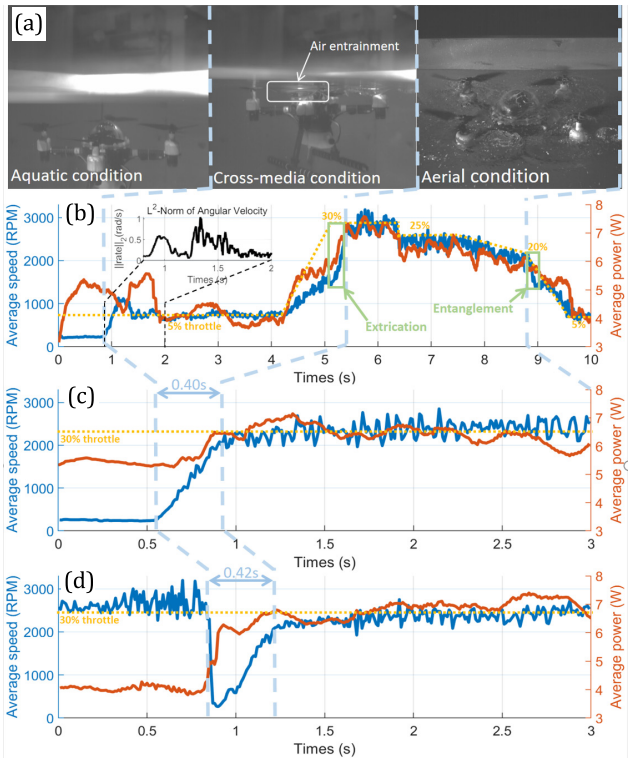

Fig. 14. Aquatic to aerial transition performance.

enter the aerial condition, indicating that the vehicle can be maneuvered completely according to aerial strategy. Conversely, it will fall back to the water surface and be entangled in the cross-medium condition, implying that the propeller will operate in a mixed water-air environment and induce air entrainment. The unstable flow field caused by air entrainment will then generate attitude jitter, resulting in greater power output, particularly when the blade is just in contact with water or the throttle is changing.

Furthermore, increasing the throttle to the extrication critical value will lift the vehicle back into the airborne condition; similarly, lowering the throttle to the entanglement critical value will drop the vehicle back into the cross-medium condition. It is worth noting that these two crucial values are not experimentally equivalent: the former is around 30% while the latter is around 20%. Furthermore, the transition from cross-medium to aerial conditions is accompanied by an abrupt shift in motor speed and jittering of the fuselage, posing a challenge to the operation. Furthermore, because the cross-medium condition would result in excessive power loss, it should be avoided as much as possible, and the method depicted in the red flow in Fig. 13, entering the aerial condition straight by inertia after leaving the water, should be a better alternative.

Propeller-induced air entrainment causes an unstable flow field [28] that leads to the chaotic motion of the vehicle at the junction of water and air, and thus propellers should be avoided working in this state as much as possible. It is a feasible strategy to breach the junction by inertia, and two specific approaches for the prototype can be considered: (i) to obtain sufficient speed underwater by the aerial mode of the propulsion unit, breach the surface inertially, and then enter the aerial condition (Fig. 14(c)); and (ii) to accelerate by the aquatic mode of the propulsion unit, and switch to the aerial mode at the breaching moment to enter the aerial condition (Fig. 14(d)). The throttle was always set at 30% during the experimental validation, which could ensure the success of the transition and no harm to the motors in the first approach. The second method can accelerate the vehicle faster with lower power consumption, which provides a longer hang time and facilities to enter the aerial condition since the aquatic mode of the propulsion unit features a better output characteristic in terms of thrust and specific thrust as shown in Fig. 12. The motor commutation process with a duration of 0.42 s is introduced into the second method, which only gaps 0.02 s compared to the acceleration time of the first one and hardly affects the transition.

This slight advantage of the first method cannot cover up its flaws in the risk of Motor damage and the high power consumption in underwater operation, and the second one is a superior way to make a seamless aquatic–aerial transition. However, the challenge with practicing this method is the determination of the mode conversion time and thrust control before and after the conversion, which will be further studied in the subsequent work.

6.3. *Aquatic maneuverability*

Snapshots of the independent thrust vectoring strategy described in Sec. 2.3 are shown in Figs. 15(b)–15(e). Even though this method is intended to be used underwater, experiments show that it can also be applied in the air (Fig. 15(e)). The thrust vectoring strategy significantly increases maneuverability when compared to the typical quadrotor maneuvering strategy (Fig. 15(a)), as shown in the yaw and horizontal movement operations. Long carbon fiber tubes connect the airframe to the UWB, which extends beyond the water, and the underwater airframe position is solved by the attitude and position of the UWB upon the surface. UWB (Nooploop Linktrack S) is used for underwater velocimetry to evaluate underwater horizontal motion performance, as shown in Fig. 15(f).

6.3.1. *Underwater yaw motion*

The results of implementing yaw motion by anti-torque (traditional quadrotor approach) and thrust vectoring, respectively, are shown in Figs. 16(a) and 16(b). Despite the fact that the airframe is intended to be under-buoyant, when yawing by anti-torque, the rate is still generated with the unavoidable upward movement, and the rate magnitude finds it difficult to reach the setpoint, confirming the issue of decoupling the yaw and the z-direction motion mentioned in Sec. 2. The tilt angle of the propulsion unit is determined by mapping the yaw joystick through Eq. (1), whose range is set to $[\frac{\pi}{6}, \frac{5\pi}{6}]$ to produce the yaw moment and a negligibly small thrust in the z-direction. This means that the yaw motion with z-position holding (Fig. 16(b), $t = 20s \sim 30s$) can be achieved by coordinating the throttle and yaw joystick displacement, whose maximum rate is roughly 4–5 times that of anti-torque.

6.3.2. *Underwater horizontal movement*

For the horizontal motion by pitch (Fig. 16(c)), the maximum body tilting angle is set to 35 (PX4 default), allowing the vehicle to travel horizontally while maintaining the

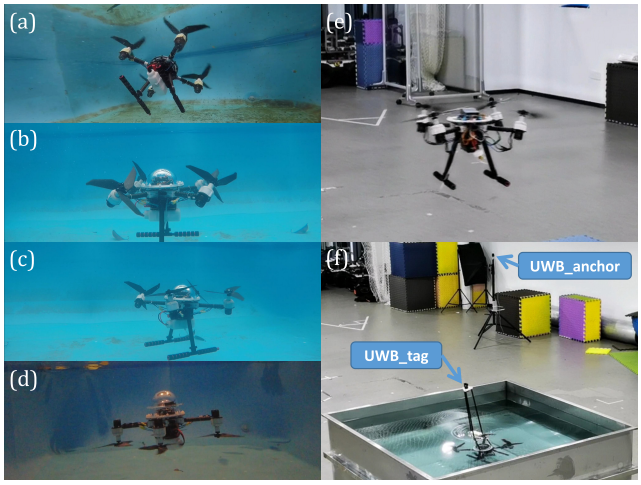

Fig. 15. Testing of the prototype.

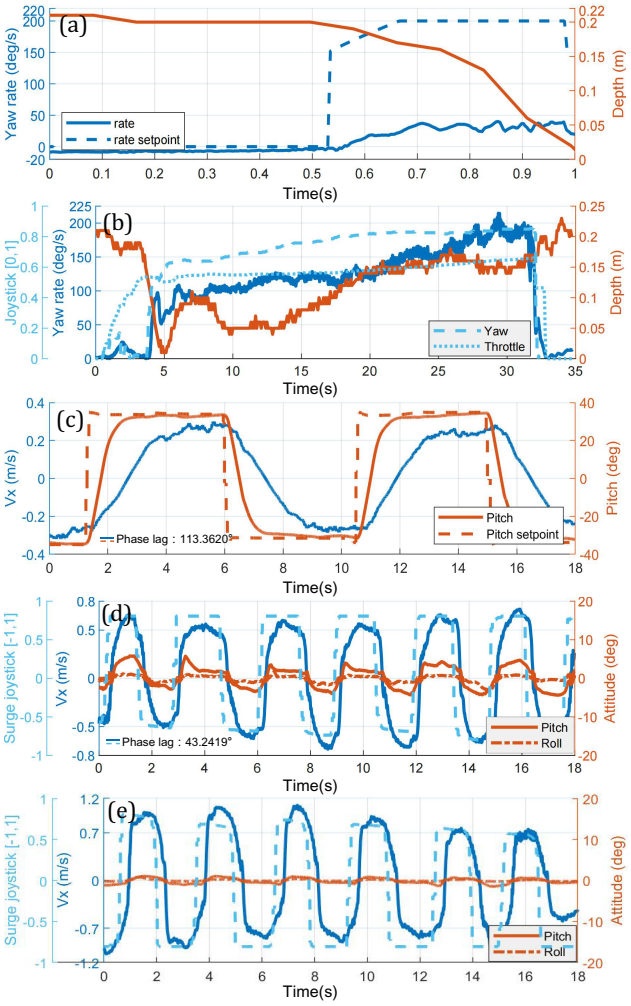

Fig. 16. Vehicle maneuverability testing.

z position at 0.3 m/s. For that by thrust vectoring (Fig. 16(d)), the input of attitude is set to 0, and the arm rotation angle mapping in the range of $[\frac{\pi}{6}, \frac{5\pi}{6}]$ is obtained by Eq. (1) in the same way as yaw movement, to provide horizontal thrust. The phase lag of v_x relative to the pitch setpoint in the former is around 113, but the phase lag of v_x relative to the joystick in the latter is approximately 43, indicating that the response speed of thrust vectoring underwater is greatly improved. However, although thrust vectoring achieved higher speeds in the experiment, this does not imply that the extreme speed is competitive. Due to the tilt arm mounting angle δ_i (Fig. 8), thrusts of each propulsion unit cannot be completely directed in the direction of motion, and partially cancel each other out, which is not the case while moving by tilting the fuselage, implying that increasing the tilt angle can result in a higher speed. Therefore, the benefit of thrust vectoring is not in fast underwater movement, but in the rapid and flexible adjustment of the direction of thrust to accomplish exact control of position and orientation.

During thrust vectoring, the attitude is perturbed as shown in Fig. 16(d). Two factors are responsible for this disruption. To begin with, there is no dedicated controller developed for thrust vectoring that limits the experimental arm rotation angle within the range of $[\frac{\pi}{6}, \frac{5\pi}{6}]$ to prevent the attitude controller from failing. Second, the dynamical coupling relationship is more complex in the underwater environment than in the air, especially for a non-streamlined fuselage, resulting in coupled attitude motion during horizontal movement. To address these issues, a dynamic mixer, as described in Sec. 2, is used to handle geometrical changes. Figure 16(e) depicts a reduction in perturbation to some extent, although complete cancellation is not achievable due to the inherent dynamical coupling problem.

6.4. *Localization performance*

Only the underwater localization experiment is carried out for the cross-medium localization system, and the functionality in the cross-medium condition will be further tested in future studies. A square tank is utilized for testing due to the lack of a technique to determine the ground truth. The vehicle is manually moved along the tank's edge to assess the performance of the odometry provided by the suggested localization approach. The localization error is less than 3 centimeters, as shown in Fig. 17(b). In addition, we also evaluated the mapping ability of the proposed algorithm, and the mapping result is shown in the Fig. 17(c). The entire algorithm is implemented using the onboard computer Nvidia Xavier NX, and the refresh rate of localization is around 20 Hz, which is sufficient for the development of underwater automatic operation.

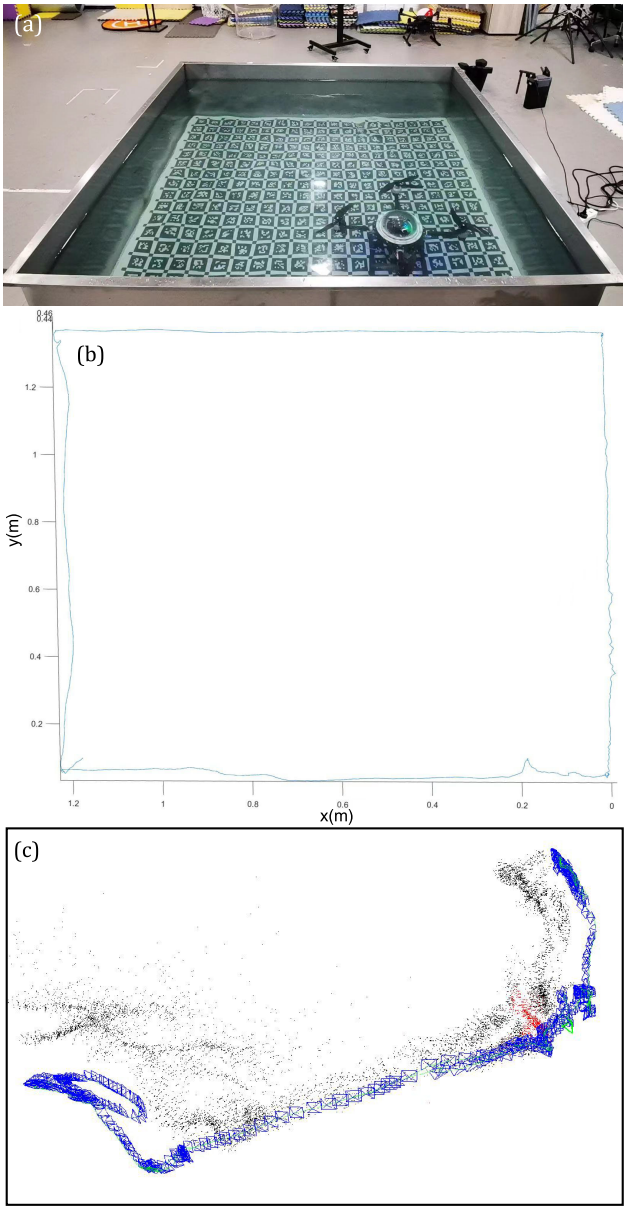

Fig. 17. Underwater Localization Performance: (a): Test Scenario. (b): Test Result in XoY Plane. (c): Underwater Mapping Result: The blue block represents the camera's field of view, while black dots represent the point cloud.

6.5. *Underwater automatic operation*

The suggested localization approach allows for fully automatic underwater traveling along preset waypoints. For instance, seven waypoints are pre-programmed, and after diving, the vehicle travels along the figure-of-eight trajectory depicted in Fig. 18(a). The cruising time is restricted to 125 s, after which the vehicle returns to water surface. The entire cruising procedure is facilitated by a real-time motion planning algorithm inherent with the PX4

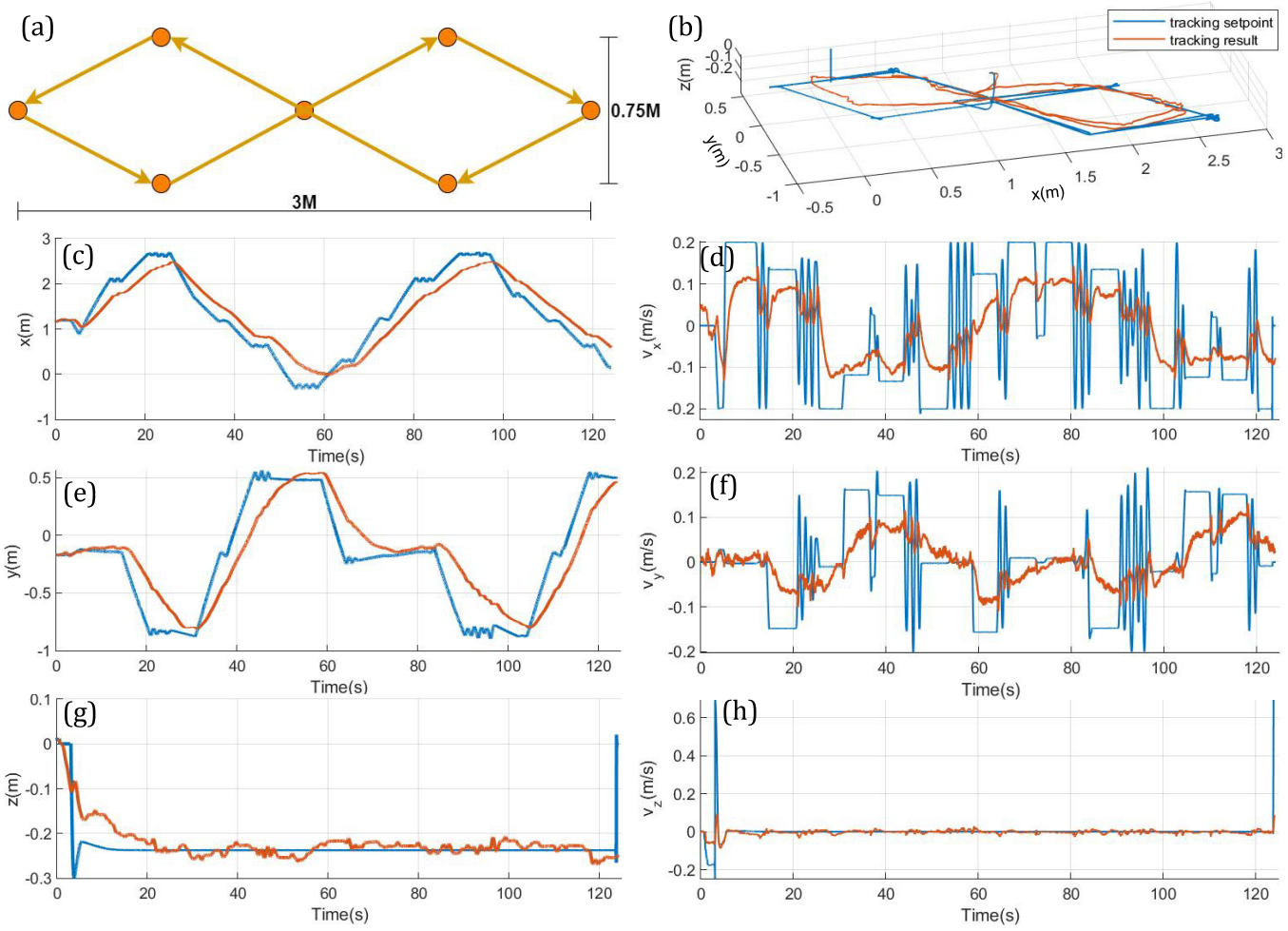

Fig. 18. Underwater Tracking Performance: (a) depicts the pre-established trajectory. (b)–(h) illustrate tracking performance, with the blue line representing the tracking setpoint and the red line showing the actual tracking result. (b) provides a 3D view of the tracking outcome. (c)–(d) Display the tracking performance in terms of position and velocity in the *x*-axis. Similarly, (e)–(f) represent the tracking performance for the *y*-axis, and (g)–(h) demonstrate the tracking performance for the *z*-axis.

firmware. A smooth trajectory with the desired position and velocity can be generated by such an inherent motion planning algorithm to link two waypoints with a straight line at a predefined cruising velocity (0.2 m/s in this practice). Once the end waypoints are obtained, the algorithm will switch to the next pair of points.

As shown in Fig. 10, the generated setpoint is fed into a cascaded PID controller with a static mixer referring to the opposite quadrotor configuration, and the PID term parameter is specifically modified for underwater operation. The final cruising performance is shown in Figs. 18(b)–18(h). The vehicle cruising speed is not able to reach the preset velocity of 0.2 m/s due to the high water drag force and poor mobility of the quadrotor configuration, as mentioned in Sec. 6.3, resulting in a margin to the position setpoint. This margin is monitored as a derailment to the desired trajectory, resulting in a fluctuation of velocity setpoint to wait for the vehicle to reach the target and rail it again. The depth hold performance is acceptable with a fluctuation range of 5 cm, as shown in Fig. 18(g), while the lateral tracking performance is poor due to the sharp turning at the corner and the aforementioned unreasonable high cruising speed given by the motion planning algorithm.

This experiment thoroughly validates the functionality of automated underwater cruising, but the performance is unsatisfactory. The factors can be summarized as:

(i) The prototype shape is not streamlined for underwater locomotion;
(ii) The quadrotor arrangement is incapable of providing sufficient locomotion excitation to accomplish agile underwater maneuvering; and
(iii) The motion planning method does not account for underwater model terms such as added mass and

drag. Further development is needed in the algorithm and structure design to improve the performance by taking the analytical model into account in the aspect of controller design and motion planning strategy, as well as shape optimization.

7. Conclusions

In this paper, we present the development of a quadrotor-based aerial–aquatic vehicle with tiltable dual-speed propulsion units. The integration of the dual-speed gearbox enhances underwater propulsion without compromising airborne efficiency. Furthermore, We introduce an independent propulsion vectoring mechanism with dynamic thrust allocation for improved aquatic agility in yaw and horizontal movement. Additionally, we discuss preliminary results on cross-medium localization and underwater cruising. Ongoing efforts focus on maximizing thrust-vectoring design benefits for attitude-independent position control. Future work includes a comprehensive hydrodynamics analysis to enhance functionality and scalability.

ORCID

Xuchen Liu https://orcid.org/0009-0008-9076-4819
Minghao Dou https://orcid.org/0009-0004-7622-3494
Ruixin Yan https://orcid.org/0009-0006-6067-0294
Dongyue Huang https://orcid.org/0009-0003-4924-1286
Songqun Gao https://orcid.org/0000-0002-2434-8656
Biao Wang https://orcid.org/0000-0001-6844-153X

References

[1] B. M. Chen, On the trends of autonomous unmanned systems research, *Engineering* **12** (2022) 20–23.
[2] Y. H. Tan and B. M. Chen, Survey on the development of aerial-aquatic hybrid vehicles, *Unmanned Syst.* **9**(3) (2021) 263–282.
[3] Z. Zeng, C. Lyu, Y. Bi, Y. Jin, D. Lu and L. Lian, Review of hybrid aerial underwater vehicle: Cross-domain mobility and transitions control, *Ocean Eng.* **248** (2022) 110840.
[4] F. M. Rockenbauer, S. L. Jeger, L. Beltran *et al.*, Dipper: A dynamically transitioning aerial-aquatic unmanned vehicle, *Robotics: Sci. Syst.* (2021), doi: 10.15607/RSS.2021.XVII.048.
[5] A. C. Horn, P. M. Pinheiro, C. B. Silva, A. A. Neto and P. L. Drews Jr., A study on configuration of propellers for multirotor-like hybrid aerial-aquatic vehicles, in *Proc. 2019 19th Int. Conf. Advanced Robotics (ICAR)* (IEEE, 2019), pp. 173–178.
[6] H. Alzu'bi, I. Mansour and O. Rawashdeh, Loon Copter: Implementation of a hybrid unmanned aquatic-aerial quadcopter with active buoyancy control, *J. Field Robot.* **35**(5) (2018) 764–778.
[7] L. Li, S. Wang, Y. Zhang, S. Song *et al.*, Aerial-aquatic robots capable of crossing the air-water boundary and hitchhiking on surfaces, *Science Robot.* **7**(66) (2022) eabm6695.
[8] Y. Chen, E. F. Helbling, N. Gravish, K. Ma and R. J. Wood, Hybrid aerial and aquatic locomotion in an at-scale robotic insect, in *Proc. 2015 IEEE/RSJ Int. Conf. Intelligent Robots and Systems (IROS)* (IEEE, 2015), pp. 331–338.
[9] K. Y. Ma, P. Chirarattananon, S. B. Fuller and R. J. Wood, Controlled flight of a biologically inspired, insect-scale robot, *Science* **340**(6132) (2013) 603–607.
[10] Y. Chen, H. Zhao, J. Mao, P. Chirarattananon, E. F. Helbling, N.-S. P. Hyun, D. R. Clarke and R. J. Wood, Controlled flight of a microrobot powered by soft artificial muscles, *Nature* **575**(7782) (2019) 324–329.
[11] Y. Bai, Y. Jin, C. Liu, Z. Zeng and L. Lian, Nezha-F: Design and analysis of a foldable and self-deployable HAUV, *IEEE Robot. Autom. Lett.* **8**(4) (2023) 2309–2316.
[12] Y. H. Tan and B. M. Chen, A morphable aerial-aquatic quadrotor with coupled symmetric thrust vectoring, in *Proc. 2020 IEEE Int. Conf. Robotics and Automation (ICRA)* (IEEE, 2020), pp. 2223–2229.
[13] Y. Chen, H. Wang, E. F. Helbling *et al.*, A biologically inspired, flapping-wing, hybrid aerial-aquatic microrobot, *Science Robot.* **2**(11) (2017) eaao5619.
[14] A. Vyas, R. Puppala, N. Sivadasan, A. Molawade, T. Ranganathan and A. Thondiyath, Modelling and dynamic analysis of a novel hybrid aerial-underwater robot-acutus, in *OCEANS 2019-Marseille* (IEEE, 2019), pp. 1–6.
[15] Y. Bi, Y. Jin, C. Lyu, Z. Zeng and L. Lian, Nezha-Mini: Design and locomotion of a miniature low-cost hybrid aerial underwater vehicle, *IEEE Robot. Autom. Lett.* **7**(3) (2022) 6669–6676.
[16] Y. H. Tan and B. M. Chen, A morphable aerial-aquatic quadrotor with coupled symmetric thrust vectoring, in *Proc. 2020 IEEE Int. Conf. Robotics and Automation (ICRA)* (IEEE, 2020), pp. 2223–2229.
[17] Y. H. Tan and B. M. Chen, Motor-propeller matching of aerial propulsion systems for direct aerial-aquatic operation, in *Proc. 2019 IEEE/RSJ Int. Conf. Intelligent Robots and Systems (IROS)* (IEEE, 2019), pp. 1963–1970.
[18] X. Liu, M. Dou, D. Huang *et al.*, TJ-Flyingfish: Design and implementation of an aerial-aquatic quadrotor with tiltable propulsion units, in *Proc. 2023 IEEE Int. Conf. Robotics and Automation (ICRA)* (IEEE, 2023), pp. 7324–7330.
[19] Y. H. Tan and B. M. Chen, A lightweight waterproof casing for an aquatic UAV using rapid prototyping, *2020 Int. Conf. Unmanned Aircraft Systems (ICUAS)* (IEEE, 2020), pp. 1154–1161.
[20] Y. H. Tan, R. Siddall and M. Kovac, Efficient aerial-aquatic locomotion with a single propulsion system, *IEEE Robot. Autom. Lett.* **2**(3) (2017) 1304–1311.
[21] Y. H. Tan and B. M. Chen, Thruster allocation and mapping of aerial and aquatic modes for a morphable multimodal quadrotor, *IEEE/ASME Trans. Mech.* **25**(4) (2020) 2065–2074.
[22] M. Ryll, H. Heinrich and P. R. Giordano, A novel overactuated quadrotor unmanned aerial vehicle: Modeling, control, and experimental validation, *IEEE Trans. Control Syst. Technol.* **23**(2) (2014) 540–556.
[23] M. Dou, X. Liu, D. Huang *et al.*, Modeling and operating point analysis for aquatic translational motion of a cross-medium vehicle, in *Proc. 42nd Chinese Control Conf.* (IEEE, 2023), pp. 1351–1357.
[24] M. Dou, X. Liu, D. Huang *et al.*, Mathematical modeling of underwater motion for a cross-medium vehicle, *Control Engineering of China*, **30**(8) (2023).
[25] T. I. Fossen, *Marine Control Systems: Guidance, Navigation, and Control of Ships, Rigs and Underwater vehicles* (Springer, Marine Cybernetics, Trondheim, Norway, 2002).

[26] D. Ji, R. Wang, Y. Zhai and H. Gu, Dynamic modeling of quadrotor AUV using a novel CFD simulation, *Ocean Eng.* **237** (2021) 109651.
[27] H. Willee, Mission mode — PX4 user guide (2023), https://docs.px4.io/main/en/flight_modes/mission.html.
[28] A. Durve and A. Patwardhan, Numerical and experimental investigation of onset of gas entrainment phenomenon, *Chem. Eng. Sci.* **73** (2012) 140–150.